Rend. Mat. Appl. (7).
Volume 40 (2019), 257 – 287

RENDICONTI DI MATEMATICA
E DELLE SUE APPLICAZIONI

Numerical investigation of the Gatenby-Gawlinski model for acid-mediated tumour invasion

Pierfrancesco Moschetta* **and Chiara Simeoni**

Abstract. *The Gatenby-Gawlinski model for the description of cancer invasion is taken into account with the aim of investigating its structural aspects. From a phenomenological point of view, that model is inspired by the Warburg effect and relies on the acid-mediated invasion hypothesis. By means of both an analytical and numerical approach, on the heels of the results available in the literature, the main purpose consists in paving the way for improving the understanding of the mechanisms the model is ruled by. We adopt a suitable numerical strategy based on a finite volume approximation and provide a space-averaged propagation speed estimate as a tool to investigate the phenomenon of traveling fronts. Simulations are performed and realistic evidence emerging from the experiments is highlighted. Afterwards, we make reasonable assumptions for justifying some system reductions leading to a simplified version and discuss the results without neglecting natural bonds with the whole system. Finally, the multidimensional environment is explored with emphasis on some important qualitative aspects strongly linked to experimental observations.*

1. Introduction

Nowadays, cancer research is one of the most active and interdisciplinary investigation fields. A lot of effort is made in order to improve the actual strategies and get significant results: this is certainly a very challenging point, but it is interesting to notice how, more and more often, new answers are developed changing the point of view the entire research is ruled by and employing approaches whose most appreciable feature is their transverse nature. In this scenario, a remarkable role is played, for instance, by the *Systems Biology* paradigm [1, 25, 26, 34], whose crucial point is the awareness that any complex biomedical problem, such as cancer, must be faced adequately considering the system as a whole, something more than the mere sum of its components, according to an holistic point of view.

This kind of approach is an example among the most interesting strategies that have spread out involving scientists from different fields and the key point, recognizable within all the modern research paths, is the requirement for relying on

2010 Mathematics Subject Classification: 35K57, 35Q92, 35C07, 65M06, 65M08, 92C15, 92C37, 92C50.

Keywords: Warburg effect, acid-mediated tumour invasion, reaction-diffusion systems, traveling fronts, wave speed estimate, finite volume/element methods, data analysis.

*Corresponding author.

mathematical modeling. As a matter of fact, applied mathematics is turning out to be a powerful tool for ensuring deeper investigations, especially in the biomedical fields, where suitable models can be developed to support experimental studies. Indeed, although such models are often subject to limitations, the awareness of their indispensability within cancer research is widely spreading, especially for the possibility of both trying and forecasting therapies [12, 16] regardless the mathematical framework complexity, which is not an essential requirement.

The focus of this article is the so-called Warburg effect [38, 39] and its mathematical modeling by means of the acid-mediated invasion hypothesis, namely the typical strategy of acidity increasing against the environment operated by tumours to regulate their growth, which is already mentioned in [9] and then popularly translated into a system of reaction-diffusion equations [11, 24], whose main feature for mathematical investigation is the existence of traveling waves [4, 5, 8, 13, 14, 15, 16, 35, 36]. Although the Gatenby-Gawlinski model as originally presented in [11, 13] is somehow outmoded, since more sophisticated systems have been introduced to account for improved approximations of realistic biomedical experiments, our interest in that context is exploring the multidimensional framework for which analytical results are neither available nor supportive.

Before starting the investigation, it is worth framing adequately the biomedical context behind the model, specifically describing the hallmarks the *Warburg effect* is characterized by. This phenomenon concerns the metabolism of cancer cells, essentially providing their glucose uptake rates: it has been firstly observed by Otto Warburg [38] in the 1920s, and afterwards confirmed through many experiments, that tumour cells tend to rely on glycolytic metabolism even in presence of huge oxygen amounts. Indeed, from a strictly biomedical point of view, it is important noticing that normal cells undergo glucose metabolism by employing oxidative phosphorylation pathways, which is the most effective process in terms of adenosine triphosphate production and requires oxygen as main resource. Tumour cells behaviour seems to forbear the conventional pathway and appeal instead to glycolysis, inducing lactic acid fermentation, a product generally released in hypoxia regime (see Figure 1).

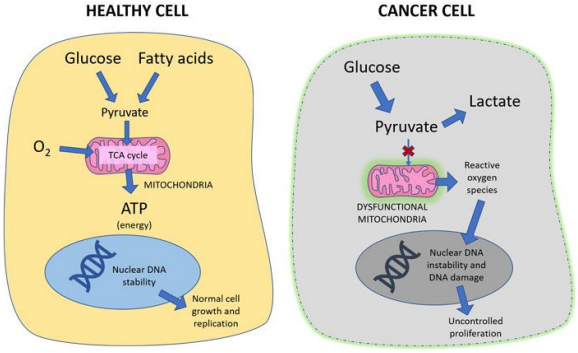

Figure 1: Different pathways of healthy and cancer cells metabolism [27].

Although the Warburg effect has been intensely studied by now, how this phenomenon happens and affects cancer proliferation is still an open problem, producing discussions about the detection of any possible advantage tumour cells might benefit from. In [33], for instance, a computational model is proposed with the aim of explaining the Warburg effect and its consequences in the tumour microenvironment, deducing the glycolytic property of tumours to proliferate in poorly vascularized tissues avoiding neo-vascularization. The transition between normal to glycolytic metabolism is object of study in [3], through a mathematical model developed to explore the Warburg effect in tumour cords: it is pointed out the capacity of tumours to lean solely on glycolysis. By exploiting a combination of modeling and in vitro experiments, instead, in [6] it is shown how cancer metabolic changes are able to define a microenvironment where the better adapted malignant cells overwhelm the others and spatial structures are created. And in [2], by means of a multiplayer game theory with specific payoff functions, the Warburg effect is approached as a sort of cooperation involving cancer cells, assuming that the public good consists in glycolysis products.

As regards the analysis carried out in this article, the above mentioned *acid-mediated invasion hypothesis* is doubtless the phenomenological key point. The crucial assumption consists in that acidification caused by lactic acid production is globally advantageous for the cancer cells population, whilst defining a toxic microenvironment for healthy cells. On that account, the original modeling based on reaction-diffusion equations developed by Gatenby and Gawlinski [11] is suitable to perform numerical investigations, because it translates the previous qualitative statements to deal with invasive species evolving and modifying within a specific microenvironment belonging to a healthy population. In that context, a novel attempt has been made to extend the analysis to the multidimensional framework, which is not deeply explored yet. Actually, in [31] an investigation of the two-dimensional context is carried out by means of an inverse problem formulation: we have explored the two-dimensional problem as well, and we have reached beyond by considering also some three-dimensional configurations [9].

The contents of this article are organized as follows. In Section 2, the general form of the model is illustrated along with its adimensionalization, and the main features of the system are considered, without neglecting the corresponding biomedical motivations. Section 3 is devoted at building a suitable numerical algorithm, based on a finite volume approximation for the spatial discretization, while a semi-implicit approach is invoked for the time discretization. In Section 4, a space-averaged wave speed approximation is derived to allow investigations of the phenomenon of traveling fronts. In Section 5, simulations are performed on the ground of the results available in the literature: the wave speed approximation is exploited to verify the existence of a stable threshold for the propagating fronts. Section 6 concerns with the possibility of assuming simplifying hypotheses in order to build a model reduction, however allowing to preserve some important qualitative features. In Section 7, the multidimensional environment is analyzed by means of a finite element approach, considering both two-dimensional and three-

dimensional simulations. Finally, in Section 8, we discuss collected results and perspectives on future research.

2. The Gatenby-Gawlinski model

The model, firstly proposed by Gatenby and Gawlinski in [11], is developed in order to reproduce cancer cells invasion within a healthy tissue, starting from a stage in which the carcinogenesis has already happened and, then, it is not further taken into account. The authors instead focus on the interactions between malignant and healthy cells populations occurring at the tumour-host interface, where a significant role is played by the lactic acid production and spreading, because of the transition towards the glycolytic metabolism.

From a mathematical point of view, dealing with a *reaction-diffusion system* is required: the unknown functions are $U(x,t)$, which stands for the healthy tissue density, the tumour cells density $V(x,t)$ and $W(x,t)$ representing the extracellular lactic acid concentration in excess, so that the systems reads

$$\begin{cases} \dfrac{\partial U}{\partial t} = \rho_1 U \left(1 - \dfrac{U}{\kappa_1}\right) - \delta_1 U W \\ \dfrac{\partial V}{\partial t} = \rho_2 V \left(1 - \dfrac{V}{\kappa_2}\right) + D_2 \dfrac{\partial}{\partial x}\left[\left(1 - \dfrac{U}{\kappa_1}\right)\dfrac{\partial V}{\partial x}\right] \\ \dfrac{\partial W}{\partial t} = \rho_3 V - \delta_3 W + D_3 \dfrac{\partial^2 W}{\partial x^2} \end{cases} \tag{2.1}$$

with initial and boundary conditions to be introduced later on. For the functions U and V a logistic growth is considered, with carrying capacities k_1 and k_2 respectively, while ρ_1 and ρ_2 are the growth rates; instead, δ_1 is a death rate proportional to W, this term being involved to reproduce healthy cells degradation due to the interactions with the lactic acid.

The structure of the degenerate diffusion term within the second equation is indeed a very interesting feature of the model (2.1) and its importance for tumour cells density is justifiable by means of biomedical arguments. As a matter of fact, the coefficient D_2 stands for a diffusion constant of the neoplastic tissue when there is a complete lack of healthy tissue. On the other hand, when the local healthy tissue concentration is at its carrying capacity, the diffusion coefficient equals zero and the cancer cells are unable to spread out. As a result, no tumour spreading is allowed unless the surrounding healthy cells concentration is no longer equal to its carrying capacity. This is aimed at simulating a realistic defense mechanism regarding tumour confinement [11, 32]: it is postulated that, for neoplastic tissue, the diffusion rate diminishes in proportion to the healthy tissue concentration, whilst diffusion is assumed to be negligible for normal tissue (that should be intended as compared to the neoplastic tissue for its mesenchymal phenotype [34]). It is important to notice that, despite its initial originality, the diffusion term pertaining to the tumour cells population inside the Gatenby-Gawlinski model (2.1) is

also one of its severe limitations, because experimental observations suggest that it should actually account for the contribution of tumor cells as well; moreover, it is reasonable to define a global density threshold, including healthy and tumour cells, which inhibits not only diffusion but also proliferation of both U and V as regulated by their combination or rather competition [10, 18].

Finally, in the third equation, a standard diffusion process with constant D_3 is considered for the spatial spreading of the lactic acid. Moreover, a growth rate ρ_3 is involved for the acid production, which is linearly proportional to V, while δ_3 is a physiological reabsorption rate.

In order to deal with more manageable quantities, it is advisable making the system (2.1) non-dimensionalized, as already done in [11], so that we have

$$\begin{cases} \dfrac{\partial u}{\partial t} = u(1-u) - duw \\ \dfrac{\partial v}{\partial t} = rv(1-v) + D\dfrac{\partial}{\partial x}\left[(1-u)\dfrac{\partial v}{\partial x}\right] \\ \dfrac{\partial w}{\partial t} = c(v-w) + \dfrac{\partial^2 w}{\partial x^2} \end{cases} \tag{2.2}$$

and the experimental domain is assumed to be the one-dimensional interval $[-L, L]$, with $t \geq 0$. This resultant version allows to operate with fewer (positive) parameters d, r, D and c, thus reducing their original range and coping with scaled functions $u(x,t)$, $v(x,t)$ and $w(x,t)$. As regards the boundary data, the homogeneous Neumann problem is contemplated for the numerical simulations.

For the one-dimensional framework, a comprehensive study of the traveling fronts associated to the Gatenby-Gawlinski model (2.1) is performed in [8] to identify the key qualitative features of wave propagation, because no rigorous proof of the existence of traveling waves seems to be presently available. By making use of *matched asymptotic expansions*, the system of traveling wave solutions with suitable asymptotic and boundary conditions is analyzed after appropriate rescaling; moreover, conditions for the appearance of a *tumour-host interstitial gap* are provided, thus confirming and extending the estimates proposed in [11, 13].
The numerical results shown in Section 5 are consistent with those illustrated in [8] and a systematic comparison is addressed in a forthcoming article, together with an application of the analytical approach to the model reduction in Section 6.

We conclude this section by mentioning that a generalized version of (2.1) and (2.2) is proposed in [24], including terms for acid-mediated tumour cells death and mutual competition between healthy and cancer cells. Other models for tumour invasion for which the existence of propagating fronts is crucial are based on combined mechanisms of extracellular matrix dynamics and haptotaxis [28, 29].

3. The numerical algorithm

We have adopted a numerical strategy based on cell-centered finite volume approximations for the spatial discretization (refer to [40], for instance). The choice of a *finite volume method* is motivated by the possibility of relying on the integral formulation of the system equations, that is a suitable ground to guarantee consistency in terms of closeness to the physics of the model.

In order to derive a semi-discrete finite volume approximation, we firstly look at the general case of a nonuniform mesh and impose that $Z_i = [x_{i-\frac{1}{2}}, x_{i+\frac{1}{2}})$ is the finite volume centered at $x_i = \dfrac{x_{i-\frac{1}{2}} + x_{i+\frac{1}{2}}}{2}$, for $i = 1, 2, ..., N$, where N is a fixed number of vertices to be selected on the one-dimensional mesh.
Let $\Delta x_i = |x_{i+\frac{1}{2}} - x_{i-\frac{1}{2}}|$ be the (variable) spatial mesh size, so that $|x_i - x_{i-1}| = \dfrac{\Delta x_{i-1}}{2} + \dfrac{\Delta x_i}{2}$ is the typical length for an interfacial interval (see Figure 2).

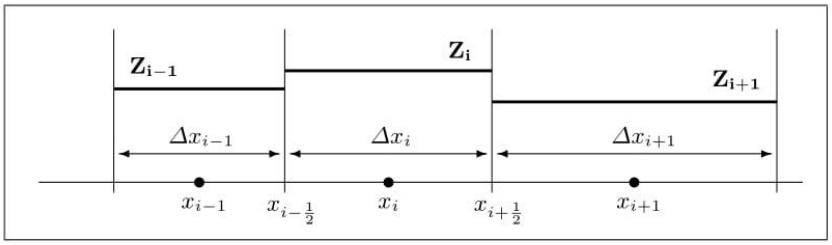

Figure 2: Piece-wise constant reconstruction on nonuniform mesh.

We start by taking into account the equation for the healthy tissue density in (2.2) and we examine its finite volume integral version,

$$\frac{1}{\Delta x_i}\int_{Z_i} \frac{\partial u}{\partial t}(x,t)\,dx = \frac{1}{\Delta x_i}\int_{Z_i} u(x,t)\big(1-u(x,t)\big)\,dx - \frac{d}{\Delta x_i}\int_{Z_i} u(x,t)w(x,t)\,dx\,,$$

which can be handled by introducing the usual notation for finite volume integral averages, namely $u_i(t) \simeq \dfrac{1}{\Delta x_i}\displaystyle\int_{Z_i} u(x,t)\,dx$, hence the semi-discrete equation reads

$$\frac{d}{dt}u_i(t) = u_i(t)\big(1-u_i(t)\big) - d\,u_i(t)w_i(t)\,. \tag{3.1}$$

Similarly, the equation for the tumour cells density in (2.2) is rewritten as

$$\begin{aligned}\frac{1}{\Delta x_i}\int_{Z_i} \frac{\partial v}{\partial t}(x,t)\,dx = {} & \frac{r}{\Delta x_i}\int_{Z_i} v(x,t)\big(1-v(x,t)\big)\,dx \\ & + \frac{D}{\Delta x_i}\int_{Z_i} \frac{\partial}{\partial x}\left[\big(1-u(x,t)\big)\frac{\partial v}{\partial x}(x,t)\right]dx\end{aligned}$$

and a suitable approach must be arranged for the finite volume integral average of the diffusion term. In particular, we proceed by evaluating the differential term at the mesh interfaces as follows,

$$\begin{aligned}
&\frac{D}{\Delta x_i}\left[\big(1-u(x_{i+\frac12},t)\big)\frac{\partial v}{\partial x}(x_{i+\frac12},t)-\big(1-u(x_{i-\frac12},t)\big)\frac{\partial v}{\partial x}(x_{i-\frac12},t)\right]\\
&\simeq \frac{D}{\Delta x_i}\left[\frac{\big(1-u_i(t)\big)\Delta x_i+\big(1-u_{i+1}(t)\big)\Delta x_{i+1}}{\Delta x_i+\Delta x_{i+1}}\cdot\frac{v_{i+1}(t)-v_i(t)}{\frac{\Delta x_i}{2}+\frac{\Delta x_{i+1}}{2}}\right.\\
&\qquad\left.-\frac{\big(1-u_{i-1}(t)\big)\Delta x_{i-1}+\big(1-u_i(t)\big)\Delta x_i}{\Delta x_{i-1}+\Delta x_i}\cdot\frac{v_i(t)-v_{i-1}(t)}{\frac{\Delta x_{i-1}}{2}+\frac{\Delta x_i}{2}}\right],
\end{aligned}\tag{3.2}$$

where the interfacial quantities are approximated by building weighted averages whose weights are the size of the adjacent finite volumes, so that $\Delta x_i/\Delta x_{i+1}$ and $\Delta x_{i-1}/\Delta x_i$ are employed at the interfaces $x_{i+\frac12}$ and $x_{i-\frac12}$, respectively. The first order derivatives of $v(x,t)$ are discretized by means of an upwind formula which makes use of the function evaluations at the neighboring vertices.
Finally, as concerns the equation for the extracellular lactic acid in (2.2), we have

$$\begin{aligned}
\frac{1}{\Delta x_i}\int_{Z_i}\frac{\partial w}{\partial t}(x,t)\,dx &= \frac{c}{\Delta x_i}\int_{Z_i}v(x,t)\,dx-\frac{c}{\Delta x_i}\int_{Z_i}w(x,t)\,dx\\
&\quad+\frac{1}{\Delta x_i}\int_{Z_i}\frac{\partial^2 w}{\partial x^2}(x,t)\,dx
\end{aligned}$$

and, by proceeding as for the previous cases, we derive the approximation

$$\frac{d}{dt}w_i(t)=c\big(v_i(t)-w_i(t)\big)+\frac{1}{\Delta x_i}\left[\frac{w_{i+1}(t)-w_i(t)}{\frac{\Delta x_i}{2}+\frac{\Delta x_{i+1}}{2}}-\frac{w_i(t)-w_{i-1}(t)}{\frac{\Delta x_{i-1}}{2}+\frac{\Delta x_i}{2}}\right].\tag{3.3}$$

Henceforward, for the sake of simplicity, the quantity Δx_i is assumed to be constant, namely $\Delta x_i=\Delta x$ for all $i=1,2,\dots,N$. Consequently, from (3.2) the semi-discrete version of the equation for the cancer cells density becomes

$$\begin{aligned}
\frac{d}{dt}v_i(t)=r\,v_i(t)\big(1-v_i(t)\big)+\frac{D}{\Delta x}&\left[\frac{\big(1-u_i(t)\big)+\big(1-u_{i+1}(t)\big)}{2}\cdot\frac{v_{i+1}(t)-v_i(t)}{\Delta x}\right.\\
&\left.-\frac{\big(1-u_{i-1}(t)\big)+\big(1-u_i(t)\big)}{2}\cdot\frac{v_i(t)-v_{i-1}(t)}{\Delta x}\right]
\end{aligned}$$

and, after some conventional manipulations, it can be rearranged to get

$$\begin{aligned}\frac{d}{dt}v_i(t) = r\,v_i(t)\big(1-v_i(t)\big) + \frac{D}{\Delta x^2}\Big[&\big(1-u_i(t)\big)\big(v_{i+1}(t)-2\,v_i(t)+v_{i-1}(t)\big)\\ &-\frac{1}{2}\big(v_{i+1}(t)-v_i(t)\big)\big(u_{i+1}(t)-u_i(t)\big)\\ &-\frac{1}{2}\big(v_i(t)-v_{i-1}(t)\big)\big(u_i(t)-u_{i-1}(t)\big)\Big].\end{aligned} \tag{3.4}$$

Finally, the equation (3.3) in the case of a uniform mesh reads

$$\frac{d}{dt}w_i(t) = c\big(v_i(t)-w_i(t)\big) + \frac{w_{i+1}(t)-2\,w_i(t)+w_{i-1}(t)}{\Delta x^2}\,. \tag{3.5}$$

It is worth noticing that approximation (3.4) exhibits a structure in which the presence of the discrete Laplace operator is recognizable, along with extra terms consisting of products of upwind discretizations. These terms arise from the degenerate diffusion in the second equation of (2.2) and, indeed, the finite volume approach we have proposed leads to a diffusion splitting by autonomously selecting the first and second order contributions. By contrast, an algebraic manipulation culminating in a early separation, as it could be done for deriving finite difference schemes [30], it would entail the necessity of relying on a central discretization for the first order terms, thus not being allowed to choose a suitable propagation direction. As a consequence, the scheme provided with central approximations would prove itself to be far less stable.

For the time discretization of the semi-discrete system obtained by grouping (3.1), (3.4) and (3.5), we employ a semi-implicit strategy considering a fixed time step Δt, so that $\Delta t = |t^{n+1}-t^n|$, for $n = 0, 1, \ldots$. In particular, the reaction terms are treated explicitly, while the differential terms on the right-hand sides are approximated implicitly, as follows,

$$\begin{cases} u_i^{n+1} = & u_i^n + \Delta t\Big[u_i^n\big(1-u_i^n\big) - d\,u_i^n w_i^n\Big] \\ v_i^{n+1} = & v_i^n + r\Delta t\,v_i^n\big(1-v_i^n\big) \\ & + D\frac{\Delta t}{\Delta x^2}\Big[\big(1-u_i^{n+1}\big)\big(v_{i+1}^{n+1}-2\,v_i^{n+1}+v_{i-1}^{n+1}\big) \\ & \qquad -\frac{1}{2}\big(v_{i+1}^{n+1}-v_i^{n+1}\big)\big(u_{i+1}^{n+1}-u_i^{n+1}\big) \\ & \qquad -\frac{1}{2}\big(v_i^{n+1}-v_{i-1}^{n+1}\big)\big(u_i^{n+1}-u_{i-1}^{n+1}\big)\Big] \\ w_i^{n+1} = & w_i^n + c\,\Delta t\big(v_i^n-w_i^n\big) + \frac{\Delta t}{\Delta x^2}\big(w_{i-1}^{n+1}-2\,w_i^{n+1}+w_{i+1}^{n+1}\big) \end{cases} \tag{3.6}$$

and Neumann-type boundary conditions $u_1^n = u_2^n$, $v_1^n = v_2^n$ and $w_1^n = w_2^n$, for $n = 1, 2, \ldots$ are also implemented. This explicit-implicit mixed approach allows

to make less expensive choices for the time step, by contrast with purely explicit algorithms which would be heavily conditioned by the restrictions that stability usually requires. The possibility of adopting fully implicit schemes has also been considered, but such an idea has not been finally taken into account since no considerable accuracy in the approximation would have been gained but an increase of the computational time.

We point out that, in order to efficiently solve the discrete system (3.6), it is useful starting from the solution u^{n+1} for the healthy tissue, whose treatment turns out to be fully explicit; afterwards, by exploiting the block-matrix structure arising from the other equations, thus producing a reciprocal independence between the solutions v^{n+1} and w^{n+1}, it is easy to go ahead solving separately the corresponding equations and getting the global approximation evaluated at the discrete time t^{n+1}. Further theoretical analysis concerning the numericsl scheme (3.6) is postponed to a forthcoming article.

4. Space-averaged propagation speed approximation

Once a suitable numerical framework has been established, the natural step to be taken in order to proceed with experiments and simulations consists in defining a useful tool for the *wave speed estimation* of the numerical solutions. As a matter of fact, the most interesting qualitative feature arising from the analysis of the solutions to system (2.2) is the detection of the *traveling fronts* phenomenon [32]. Therefore, trying to quantify the associated wave speed becomes a necessary path to follow for verifying the existence of an asymptotic threshold.

With the aim of providing a numerical approximation for the wave speed at time t^n, we employ a space-averaged estimate according to the strategy proposed in [22] and successfully applied to the case of a reactive version of the Goldstein-Kac model for correlated random walk in [20, 21]. This is an original attempt within the theory of reaction-diffusion systems, being borrowed from the original field of conservation laws, and it turns out to be a robust landmark in the current mathematical context as well.

To provide the main analytical concepts behind the numerical formulation of the wave speed estimation, we briefly derive its analytical counterpart by means of some standard manipulations. Let ϕ be a differentiable function describing the traveling front profile, then we can write

$$\begin{aligned}\int_{\mathbb{R}} \big[\phi(\xi+h)-\phi(\xi)\big]\,d\xi &= h\int_{\mathbb{R}}\int_0^1 \frac{\partial\phi}{\partial\xi}(\xi+\theta h)\,d\theta\,d\xi = h\int_0^1\int_{\mathbb{R}} \frac{\partial\phi}{\partial\eta}(\eta)\,d\eta\,d\theta \\ &= h\int_0^1 \big[\phi(+\infty)-\phi(-\infty)\big]\,d\theta = h\big(\phi_+-\phi_-\big),\end{aligned}$$

where $h>0$ is an increment, ϕ_+ and ϕ_- are assumed to be (different) asymptotic states for the function ϕ (heteroclinic traveling fronts). At this stage, setting

$h = -s\Delta t$, we deduce the following integral equation for the wave speed

$$s = \frac{1}{[\phi]\Delta t} \int_{\mathbb{R}} \big[\phi(\xi) - \phi(\xi - s\Delta t)\big] d\xi \,,$$

by imposing the synthetic notation $[\phi] \coloneqq \phi_+ - \phi_-$.

We recall that a traveling front profile is related to the actual solution through the change of variable $\xi = x - s\,t$, so that $\phi(\xi)$ corresponds to $v(x,t)$ if we focus on the invasion front at speed s of the tumour cells density, for instance. Hence, in discrete form, the space-averaged wave speed estimation for $v(x,t)$ over a uniform spatial mesh at time t^n is given by

$$s^n = \frac{\Delta x}{[\phi]\Delta t} \sum_{i=1}^{N} \big(v_i^n - v_i^{n+1}\big), \tag{4.1}$$

with ϕ_+ and ϕ_- that are prescribed as stationary states of the equation for $v(x,t)$ inside the dynamical system underlying (2.2). It is important to emphasize that the strength of estimate (4.1) lies in its absolute independence from the dynamics of the solutions provided by (2.2), thus being always numerically computable.

5. One-dimensional simulation results

In order to validate the numerical algorithm, numerical simulations have been performed using the scheme (3.6), together with formula (4.1) for the wave speed estimation. In this section, we are interested in recovering computational results described in the literature [8, 11, 13], therefore the experiments are carried out with the scaled parameters available in [24], as listed in Table 1, and then with the parameters in [8], as listed in Table 2. Besides the quantities already discussed for the model presentation in Section 2, we assume T as the final time instant, while the spatio-temporal mesh is built by fixing $\Delta x = 0.005$ and $\Delta t = 0.01$.

Table 1: Numerical values for the simulation parameters [24]

d	**r**	**D**	**c**	**L**	**T**
$\{0.5, 1.5, 2.5, 3, 12.5\}$	1	$4 \cdot 10^{-5}$	70	1	20

For the choice of the initial profiles, according to what proposed in [24], a piecewise linear decreasing density is taken into account for the cancer cells extending out from its core, where $v = 1$, and getting towards zero; for the healthy cells density, the starting graph is simply obtained through a reflection, by imposing a complementary behaviour with respect to the cancer cells density; finally, the extracellular lactic acid concentration is initially equal to zero. The corresponding graphs are shown in Figure 3.

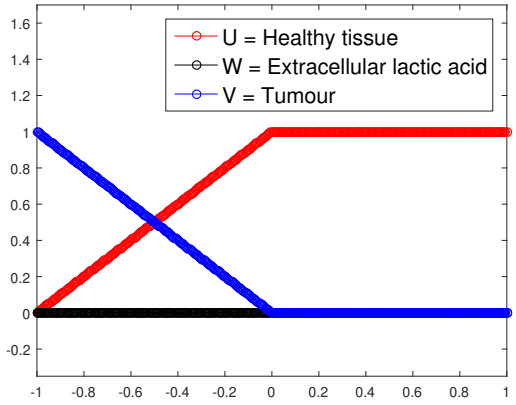

Figure 3: Graphs of the initial profiles for the numerical experiments.

The simulation results exhibit basically two different kinds of behaviours, both reported in Figure 4, which are regulated by the parameter d measuring the destructive influence of the environment acidity on the healthy tissue, and so taken as an indicator of the tumour aggressiveness. From a qualitative point of view, all solutions evolve as forward propagation fronts moving from left to right with positive wave speed. The plot shown in Figure 4(A) corresponds to a phenomenological regime known as *heterogeneous invasion*, which turns out to happen when the condition $d < 1$ is verified. It is characterized by the coexistence of tumour and healthy tissue behind the wavefront, because a fraction of normal cells survives to the chemical action of the tumour thanks to low sensitivity to the environment acidity. We remark that the boundary data considered in [8] are slightly different from those adopted for our numerical simulations, but the model dynamics implies that acid concentration immediately attains its carrying capacity at the left-hand boundary, and finally the level of the healthy cells density is exactly $1 - d$ in the purely heterogeneous case.

On the other hand, when $d >> 1$, a different evolution shape takes place, the so-called *homogeneous invasion* depicted in Figure 4(D), that is the most aggressive configuration. Indeed, the healthy tissue is being completely destroyed behind the advancing tumour cells wavefront because of the high level of acidity induced into the environment. A narrow overlapping zone actually persists for increasing values of $d > 1$, which produces *hybrid configurations* as shown in Figure 4(B) and Figure 4(C), but it reduces progressively as forcasted in [8]. A remarkable feature of the last configuration is the presence of a *tumour-host hypocellular interstitial gap*, namely a separation zone between the healthy and cancer cells populations. Such prediction, initially a mere mathematical result provided by the model, has been experimentally verified: its detection, in both unfixed in vitro experiments and

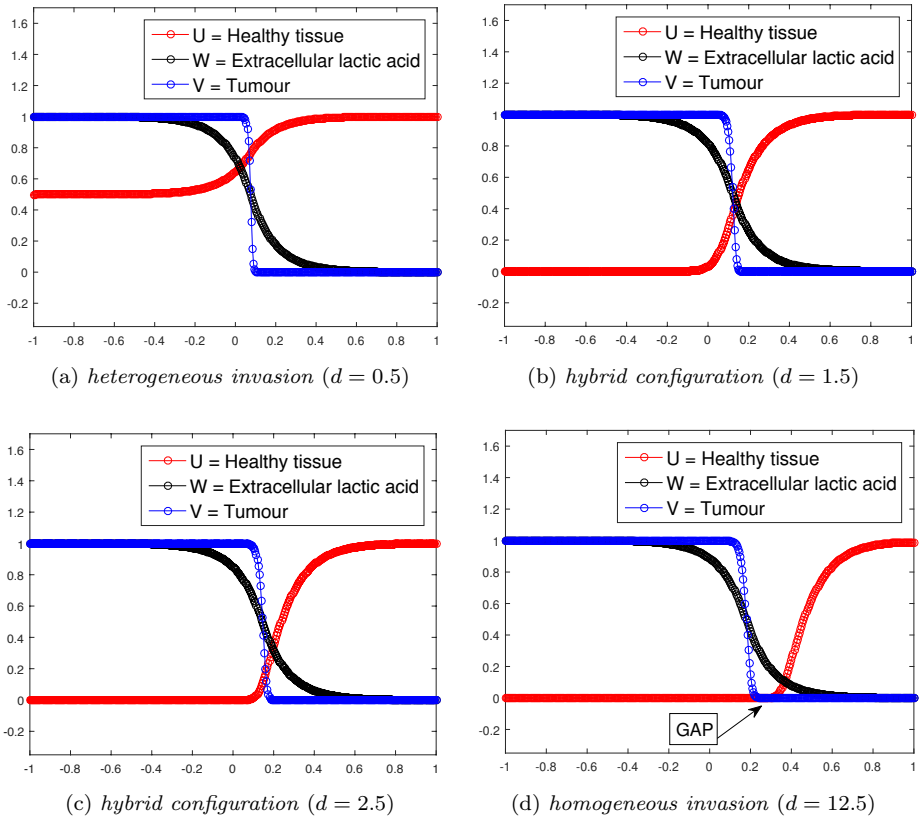

(a) *heterogeneous invasion* ($d = 0.5$)

(b) *hybrid configuration* ($d = 1.5$)

(c) *hybrid configuration* ($d = 2.5$)

(d) *homogeneous invasion* ($d = 12.5$)

Figure 4: Different configurations of the numerical solution: comparison between heterogeneous evolution (A) and existence of the spatial interstitial *gap* within the homogeneous evolution (D).

in flash-frozen tissues, has provided stronger evidence to claim this phenomenon authentication [11]. Finally, as regards the lactic acid concentration, in all cases it tracks the tumour front with a smoother profile. These results are in agreement with the corresponding records provided in [24], aimed at recovering the dynamics firstly analyzed in [11].

From a mathematical point of view, the strong dissimilarity in terms of steepness of the wave profiles for the healthy and tumours densities observed in Figure 4 is justified by the fact that somehow U inherits the (parabolic) regularity of the acid concentration W through the reaction term, whereas the diffusion constant D of the neoplastic tissue is typically very small (refer to Table 1). As a matter of fact, when passing from the system (2.1) to its non-dimensionalized version (2.2),

that parameter is deduced as $D = D_2/D_3$ and it is physically relevant to assume that D_3 is much larger than D_2. Therefore, the tumour propagating front V is normally steeper, despite its diffusivity (hindered by U through a degenerate factor) is selected as the driving mechanism of invasion, since no diffusion is considered for the healthy cells due to their epithelial phenotype [34]. Indeed, the wavefront U fails to keep its regularity once the equation for W is removed from system (2.1), as demonstrated numerically in Figure 10 for the reduced model (2.2) in Section 6. Another effect on the shape of the wave profiles can be appreciated dealing with the adimensional parameter r, which is expected to be greater than 1 since deduced as $r = \rho_2/\rho_1$ from physical considerations (we report in Figure 5 the numerical simulation of an experimental case discussed in [8], for example).

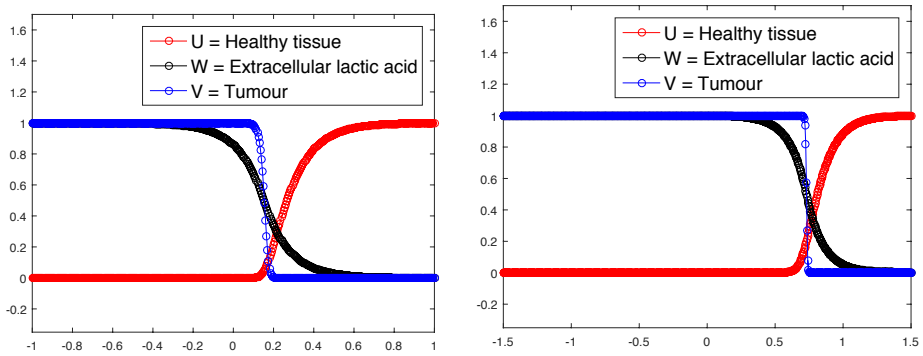

(a) *moderate growth* ($r = 1$) (b) *uncontrolled growth* ($r = 10$)

Figure 5: Qualitative analysis of tumour fronts steepness and spatial invasion as function of the adimensional growth rate (for $d = 3$).

We have attempted a qualitative comparison with the analytical results in [8] by computing numerical solutions using the parameters listed in Table 2. In particular, we are interested in tracking the formation of the interstitial *gap*, whose appearance is expected for $d > 2$ (in which case its size can also be estimated).

Table 2: Numerical values for the simulation parameters [8]

d	**r**	**D**	**c**	**L**	**T**
$\{1.5, 2.5, 4\}$	1	$4 \cdot 10^{-5}$	2	5	20

The numerical simulations reported in Figure 6 actually corroborate such prediction, although some discrepancies emerge concerning the smoothness of the wave profile for the healthy cells density, thus determining a smaller size for the *gap*

separating the host and tumour populations. Besides the effects of a bigger diffusion constant D for the tumour cells, which slightly smooths out the steepness of the propagating fronts, we must recall that the analysis in [8] is based on asymptotic expansions and, therefore, solely the leading terms contribute to shape the solution profiles (this comment applies also to Figure 5). These observations motivated the importance of undertaking a more rigorous and systematic comparison, whose conclusions are committed to a forthcoming article.

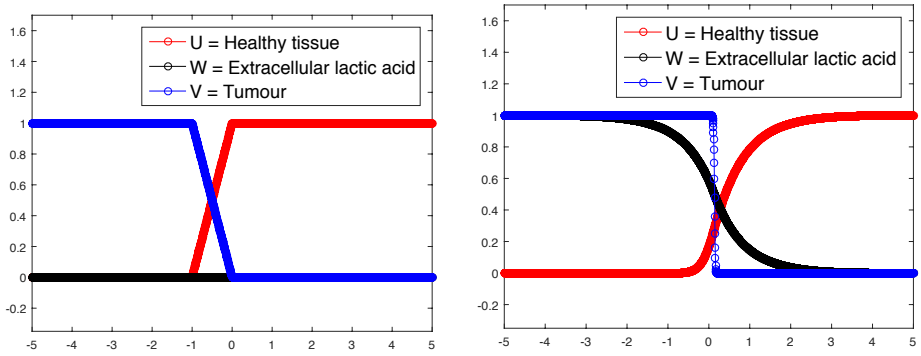

(a) *initial profiles*

(b) *hybrid configuration* ($d = 1.5$)

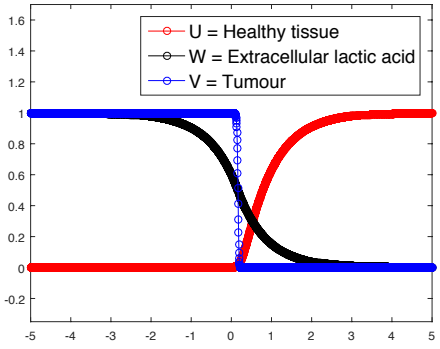

(c) *threshold regimes* ($d = 2.5$)

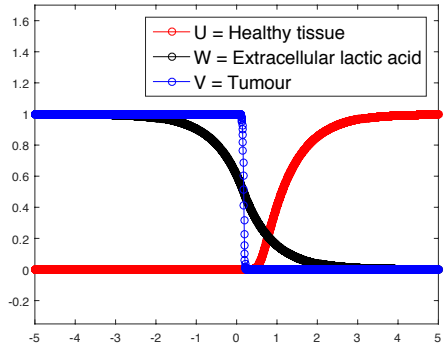

(d) *homogeneous invasion* ($d = 4$)

Figure 6: Numerical simulation of the spatial interstitial *gap* formation from heterogeneous evolution (B) to homogeneous invasion (D).

As already mentioned above, the existence of propagating fronts is a key point for our investigation and information about their wave speed is crucial. In order to quantify these values, we take advantage of the space-averaged propagation speed approximation (4.1) and we apply it to better understand the wavefronts behaviour of the Gatenby-Gawlinski model. For instance, graphs related to the

heterogeneous invasion are considered: the plot proposed in Figure 7(A) is meant for capturing front evolution starting from the initial profile and, by means of different colors, the tumour cells density function is plotted at different times until it reaches the shape of a propagating front defined by a stable wave speed. The graph in Figure 7(B) shows the discrete wave speed estimate (4.1) computed as a function of time, and it is possible to appreciate the convergence towards the asymptotic threshold; furthermore, it is easy to verify that a small waiting time is required before achieving an asymptotic value, that is a common feature of theories involving traveling fronts, simply recognizable by dealing with scalar problems. An analogous graph, of course, can be plotted in the homogeneous invasion case.

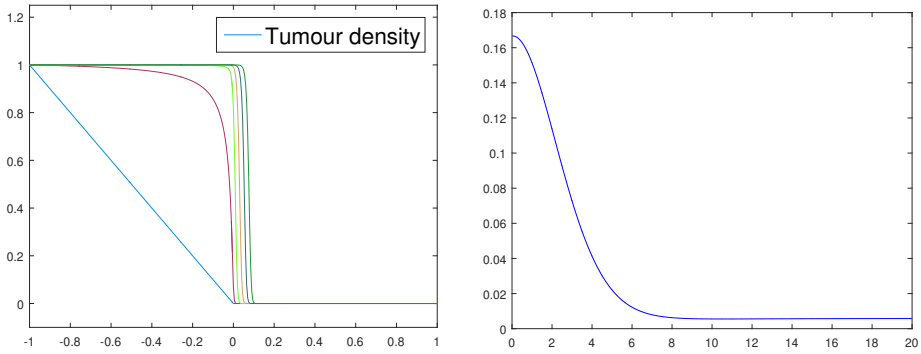

(a) *front evolution* (b) *wave speed estimates*

Figure 7: Traveling fronts investigation in the heterogeneous invasion case: the tumour density profile is plotted at six equally spaced time instants (A), together with the space-averaged propagation speed approximations as a function of time (B).

It is presently useful recalling the results of analytical asymptotic wave speed estimates provided in [24]. In Table 3 the discrete asymptotic wave speed approximations issued from (4.1) are listed in order to make a comparison: in both the homogeneous and heterogeneous cases, the relative error we get is sufficiently small to infer that numerical values are very close to the corresponding quantities computable by using the analytical formulations available in [24]. Moreover, it is interesting to notice that, at least in the homogeneous case, the wave speed prediction $s \approx 2\sqrt{Dr}$ perfectly matches the analytical formula already known for the Fisher-KPP equation [17, 37].

Table 3: Comparison between analytical wave speed formulations [24] and the numerical estimates issued from (4.1).

investigation case	**numerics**	**analytical wave speed**	**relative error**
homogeneous	0.0124	$s \approx 2\sqrt{Dr} = 0.0126$	0.0159
heterogeneous	0.0058	$s \approx \sqrt{2Ddr} = 0.0063$	0.0794

6. A useful model reduction

Once that our numerical strategy and the space-averaged propagation speed estimate have been tested, we proceed by setting a simplified version of the model. The purpose consists in carving a more approachable structure to pursue analytical investigations, trying to set ground rules both for a better mathematical understanding and, as much as possible, for keeping accuracy with respect to the original biomedical phenomena. Therefore, assuming the condition $w = v$ inside the system (2.2), we get a reduction that holds only two equations, namely

$$\begin{cases} \dfrac{\partial u}{\partial t} = u(1-u) - duv \\ \dfrac{\partial v}{\partial t} = rv(1-v) + D\dfrac{\partial}{\partial x}\left[(1-u)\dfrac{\partial v}{\partial x}\right] \end{cases} \tag{6.1}$$

and the corresponding homogeneous Neumann boundary data. Such a simplification is achievable taking into account the limit as the parameter c approaches the infinity inside the third equation of the full model (2.2), and that is motivated by the similarity between tumour cells and lactic acid evolution profiles (see Figure 4).

An interesting analysis can be performed from the graph depicted in Figure 8, where the heterogeneous case is considered as an example: for each choice of the c value, the corresponding propagation speed approximation for the tumour cells density front provided by the Gatenby-Gawlinski model (2.2) is reported, as well as the (constant) wave speed estimate for the simplified model (6.1).

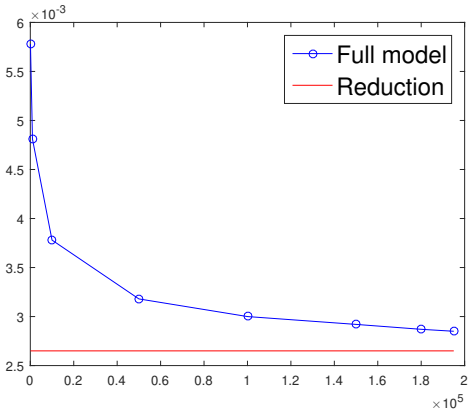

Figure 8: Wave speed estimates (blue circles) for increasing c values within the full model (2.2) and wave speed estimate (red line) provided by the simplified model (6.1).

Because this quantity is an asymptotic threshold for the full model, by increasing the c value a convergence towards the asymptotic regime is expected. At this stage, a further discussion is required since, on the one hand, it is possible to appreciate the convergence, but on the other hand we easily infer that the statement $w = v$ prevents the reduction from keeping the same wave speed produced by the complete model, thus exhibiting a quantitative mismatch. Specifically, the wave speed computed for the simplified model turns out to be smaller than the asymptotic value achieved by the full model. Such behaviour can be explained noticing that the standard diffusion of the lactic acid concentration in the third equation of (2.2) actually makes it easier to spread for the tumour cells, whose density expansion already relies on the degenerate diffusion term. As a consequence, the tumour spreading is slower for the reduced model (6.1), being no longer sustained by two distinct diffusion mechanisms.

The next step consists in testing numerically our model adjustment by using the same initial profiles (see Figure 3) and parameters (see Table 1) as for the previous simulations of the standard version in Section 5, but omitting the equation for the lactic acid concentration whatever concerns, as shown in Figure 9.

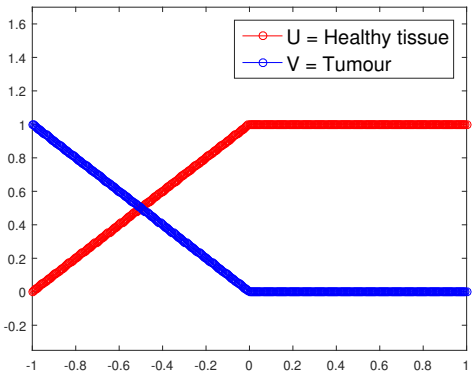

Figure 9: Graphs of the initial profiles for the simplified model.

The reduced system (6.1) is still able to reproduce important qualitative features of the full version (2.2), as it can be detected in Figure 10, and what is essential for performing a consistent mathematical analysis of the mechanisms underlying the Gatenby-Gawlinski model is the propagating fronts structure. The plots, for both the heterogeneous and homogeneous cases, exhibit similar qualitative behaviours compared to the analogous graphs in Figure 4, although some quantitative differences are obviously detectable.

In order to ensure a better understanding of the dynamics under investigation, for completing the analysis of the heterogeneous case, it is useful to report the same plots as previously shown in Figure 7 but contextualized in the model reduction framework. The front evolution for the tumour cells density is plotted in

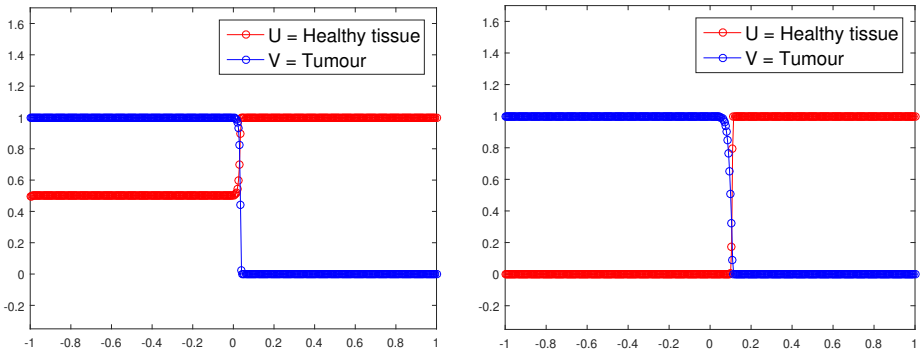

(a) *heterogeneous invasion* (b) *homogeneous invasion*

Figure 10: Comparison between two different regimes of the numerical solutions for the reduced model configuration.

Figure 11(A) and the discrete wave speed estimates are taken into account in Figure 11(B). Despite the wave speed threshold has changed with respect to the value for the full system in Figure 7(B), the model reduction upholds the same qualitative structure: indeed, the traveling fronts formation is still observable as well as the wave speed convergence towards a stable default value. Therefore, the transition occurring within the full model (2.2) as the c value approaches infinity does not prevent the system from keeping its mathematical features. However, we point out that the *gap* formation is no longer recognizable for the simplified model (6.1), and indeed in Section 5 we have already observed a delay in its appearance for higher values of the c parameter from Figure 4 with respect to Figure 6.

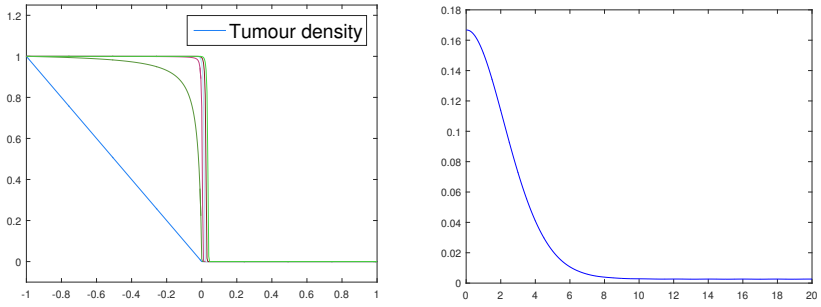

(a) *front evolution* (b) *wave speed estimates*

Figure 11: Traveling fronts investigation in the heterogeneous invasion case for the reduced model: the tumour density profile is plotted at six equally spaced time instants (A), together with the space-averaged propagation speed approximations as a function of time (B).

Therefore, we can conjecture that for its detection assuming an independent evolution for the lactic acid concentration is needed. That is why, relying on the complete model is required in order to seize the whole biomedical phenomenon, regardless of any employable reductions for performing further mathematical analysis.

7. Multidimensional simulations

Henceforward, the analysis is carried out on the ground of two-dimensional and three-dimensional domains. The main purpose consists in exploring the multidimensional framework, both for recovering the qualitative features already exhibited in the one-dimensional context and for better investigating the phenomenon of the *gap* formation, along with its geometry and evolution. For the numerical strategy, the finite element method [30] has been employed, due to its versatility in dealing with more complex geometric domains. Another advantage of this approach lies in avoiding specific treatment for the boundary conditions, which are automatically incorporated within the *weak formulation* of the system (refer to [31] for a similar methodology). Specifically, we have used *Lagrange P2 finite elements* for the numerical functions, while triangular and tetrahedral meshes have been adopted for two-dimensional and three-dimensional simulations, respectively (see Figure 12).

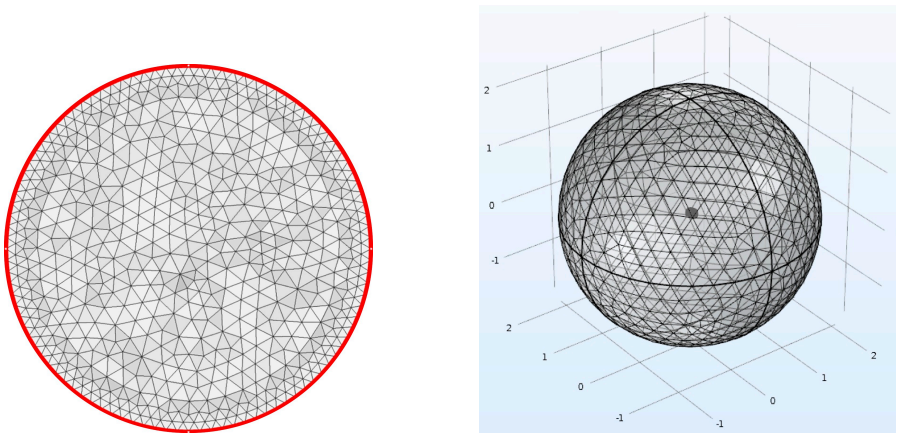

(a) *two-dimensional mesh* (b) *three-dimensional mesh*

Figure 12: Finite element triangular (A) and tetrahedral (B) meshes for radially symmetric experimental domains.

We proceed to write the multidimensional non-dimensionalized Gatenby-Gawlinski

model, namely the generalized version of system (2.2), as follows

$$\begin{cases} \dfrac{\partial u}{\partial t} = u(1-u) - duw \\ \dfrac{\partial v}{\partial t} = rv(1-v) + D\,\nabla\cdot\big[(1-u)\nabla v\big] \\ \dfrac{\partial w}{\partial t} = c(v-w) + \nabla^2 w \end{cases} \tag{7.1}$$

which is defined for some time interval $(0,T)$ and over a suitable domain $\Omega \subset \mathbb{R}^m$, $m = 2$ or 3, so that the differential operators are $\nabla = (\partial/\partial x_1, ..., \partial/\partial x_m)$ and $\nabla^2 = \sum_{i=1}^m \partial^2/\partial x_i^2$, with $m = 2$ or 3. Afterwards, let us assume that V denotes some functional space relevant to (7.1), then a weak solution $(u, v, w) \in V \times V \times V$ is a triplet of functions that satisfies, for all test functions $(g_1, g_2, g_3) \in V \times V \times V$, the following system

$$\begin{cases} \displaystyle\int_\Omega \left(\frac{\partial u}{\partial t} g_1 - u(1-u)g_1 + duwg_1 \right) d\mathbf{x} = 0 \\ \displaystyle\int_\Omega \left(\frac{\partial v}{\partial t} g_2 - rv(1-v)g_2 + D(1-u)\nabla v \cdot \nabla g_2 \right) d\mathbf{x} = 0 \\ \displaystyle\int_\Omega \left(\frac{\partial w}{\partial t} g_3 - c(v-w)g_3 + \nabla w \cdot \nabla g_3 \right) d\mathbf{x} = 0 \end{cases} \tag{7.2}$$

and the homogeneous Neumann boundary conditions are directly built into (7.2).

The above mentioned weak formulation of system (7.1) is needed to establish the mathematical context for performing simulations by using the COMSOL Multiphysics environment – https://www.comsol.it/

7.1. Two-dimensional experiments

The first important step is certainly trying to reproduce the two different kinds of tumour invasion previously described in Section 5. As concerns the domain, we consider the 2-ball of radius R centered at the point C, namely $\Omega = \overline{B_R(C)}$, such a choice for the geometry being inspired by the circular *Petri dish* widely employed in biology for cell cultures (see Figure 13). For instance, we have taken $R = 8$ and $C = (0, 0)$ as simulation parameters.

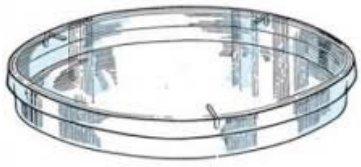

Figure 13: Sample of a circular *Petri dish* for cell cultures.

For the initial profiles, we assume the evolution of a cancerous peak located in the neighborhood of the origin and a complementary shape for the healthy cells density (see Figure 14), while the extracellular lactic acid concentration is initially assumed equal to zero. For $\mathbf{x} \in \Omega$, the corresponding functions are

$$u(\mathbf{x},0) = 1 - \frac{\exp(-\|\mathbf{x}\|^2)}{\sqrt{\pi}}, \quad v(\mathbf{x},0) = \frac{\exp(-\|\mathbf{x}\|^2)}{\sqrt{\pi}}, \quad w(\mathbf{x},0) = 0\,. \tag{7.3}$$

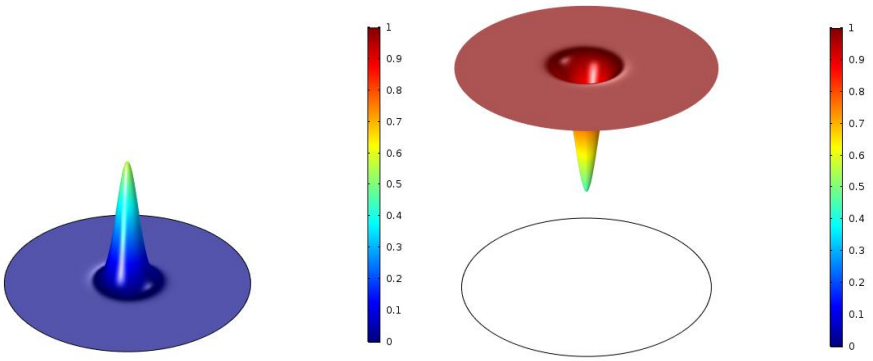

(a) *tumour cells initial profile* (b) *healthy cells initial profile*

Figure 14: Plots of the initial profiles for tumour and healthy cells densities.

Numerical simulations have been performed until $T = 13$ and the time instant $T = 6$ has been selected for checking the progress of plots also at an intermediate stage. The other simulation parameters are summarized in Table 1.
From now on, we decide to omit graphic information about the lactic acid concentration, having again recognized a persistent similarity with the behaviour of the tumour cells density (refer also to Figure 4).

The homogeneous invasion, which is expected to characterize the solutions to system (7.1) for $d > 1$, is the first case to be examined: Figure 15 and Figure 16 depict the related trends for tumour and healthy cells densities, respectively.
Starting from the graphs at the intermediate time instant, reported in Figure 15(A) and Figure 16(A), the qualitative dynamics shows clearly the initial cancerous peak growing and spreading out at the expense of the local healthy tissue. Then, the tumour invasion gradually extends towards the outermost regions of the domain (see Figure 15(B)), where the healthy cells density is finally being confined (see Figure 16(B)). It is therefore confirmed that the homogeneous invasion is the most aggressive situation, due to the complete annihilation of healthy cells behind the advancing radially headed cancerous core.

As concerns the case of heterogeneous invasion, namely for $d < 1$ into (7.1), we focus on the healthy cells density evolution (see Figure 17) but omit reporting plots

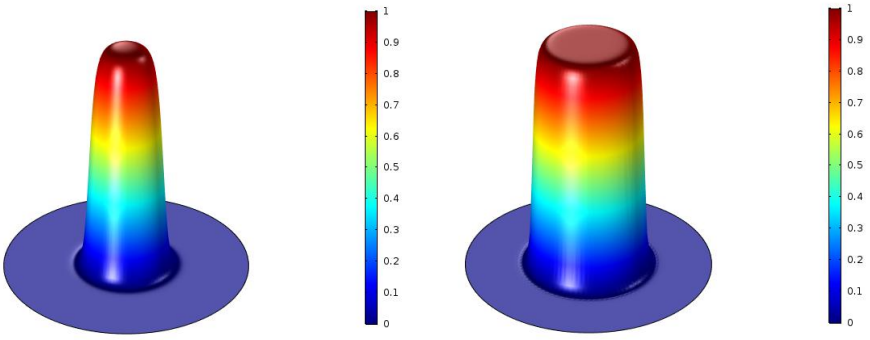

(a) *intermediate time* (b) *final time*

Figure 15: The homogeneous invasion: tumour cells density evolution at two different time instants $T=6$ (A) and $T=13$ (B).

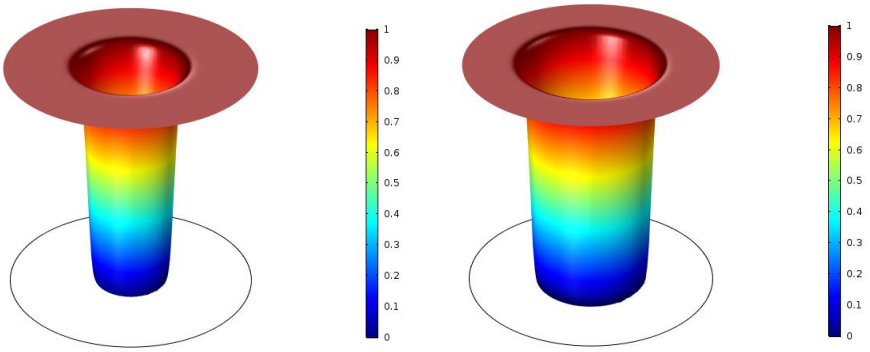

(a) *intermediate time* (b) *final time*

Figure 16: The homogeneous invasion: healthy cells density evolution at two different time instants $T=6$ (A) and $T=13$ (B).

related to the cancerous pick spreading, which turns out to be very similar to the counterpart in Figure 15 for the homogeneous configuration. As a matter of fact, it is possible to infer that the local healthy tissue is not being completely repulsed by the tumour, in contrast to what observed in Figure 16 because healthy cells are destroyed through the strong effect of the lactic acid concentration. Figure 17 shows instead that the healthy cells density reaches an asymptotic threshold within the inner region of the experimental domain, where the cancerous core is already detectable.

On the heels of the results available in the one-dimensional framework (refer to Section 5), the essential qualitative difference arising when comparing the two kinds of tumour invasion lies in the coexistence of healthy and cancer cells on one

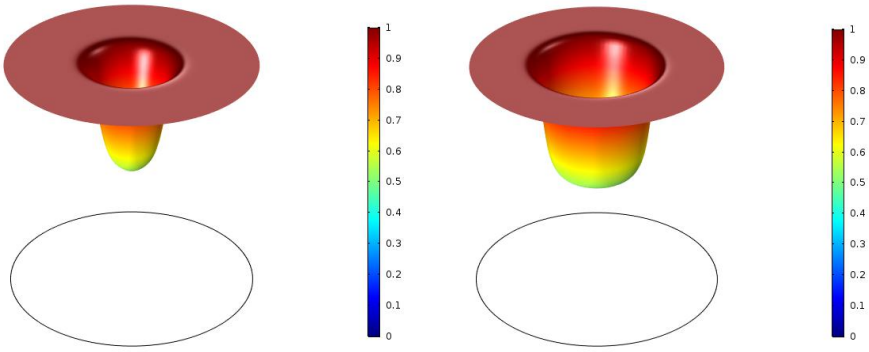

(a) *intermediate time* (b) *final time*

Figure 17: The heterogeneous invasion: healthy cells density evolution at two different time instants $T=6$ (A) and $T=13$ (B).

side (heterogeneous invasion), and the annihilation of the local healthy tissue out of the cancerous core on the other side (homogeneous invasion). However, there is something more to be evaluated: in the homogeneous case, we have appreciated that there is not intersection between healthy and tumour cells densities, as shown in Figure 4(B). Specifically, we have recognized the existence of a spatial interstitial *gap*, and we aim at detecting an analogous phenomenon within the two-dimensional context as well. To accomplish this assignment, the healthy and tumour cells densities have been plotted simultaneously and a bird-eye viewpoint is required to investigate the circular crown placed between the advancing tumour front and the retiring healthy tissue (see Figure 18). On the one hand, it is possible to appreciate the *gap* formation around the cancerous pick for the homogeneous invasion, as exhibited in Figure 18(B): a smaller blue ring, corresponding to a null density zone, is recognizable within the circular crown located between the fronts, confirming that no intersection is allowed in this aggressive regime. On the other hand, for the heterogeneous invasion, Figure 18(A) shows that healthy and tumour cells densities are actually conflated in the area lying between the fronts.

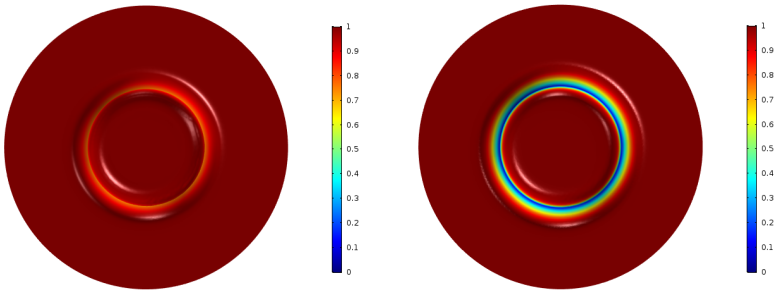

(a) *heterogeneous invasion* (b) *homogeneous invasion*

Figure 18: Identification of the two-dimensional *gap* formation for the homogeneous case (B) with respect to the heterogeneous case (A).

Finally, in order to further investigate the *gap* formation for the case of homogeneous invasion, we build a more complex configuration for the initial profiles made of three distinct cancerous peaks, by suitably rearranging the formulation (7.3). We report in Figure 19 the simultaneous plots of healthy and tumour cells densities at different time instants, by adopting the bird-eye viewpoint. We skip over the details concerning the single densities and we exploit Figure 19 both for analyzing the *gap* evolution and for qualitatively interpreting the resultant dynamics of the fronts. In Figure 19(A), we notice the formation of three blue rings characterized by null densities around the cancerous circular crowns; then, by means of two intermediate evaluations (see Figures 19(B) and 19(C)), it is shown how these rings gradually increase their size and are opening, as the corresponding cancerous peaks are colliding and going into meltdown; eventually, once the novel tumour core is well-defined, as exhibited in Figure 19(D), the resultant *gap* consists of a single contour cordoning off the cancerous crown from the surrounding marginal area, where the local healthy tissue is regressing.

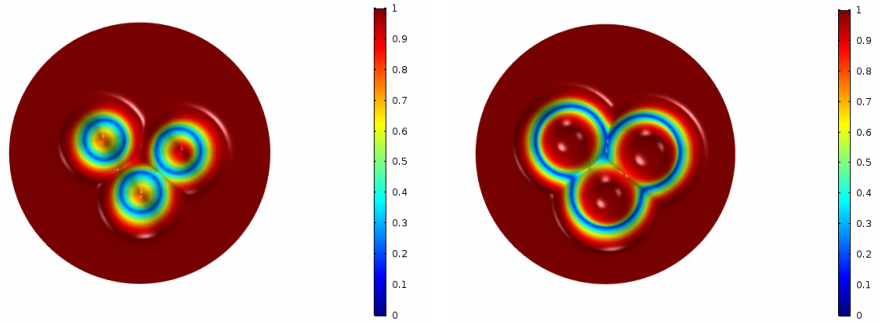

(a) *initial configuration* (b) *first intermediate time*

(c) *second intermediate time* (d) *final configuration*

Figure 19: The homogeneous invasion: formation and evolution of a two-dimensional *gap* from three initially distinct cancerous peaks.

We conclude this section by remarking that, despite the triangular arrangement of the finite element meshes (see Figure 12(A)), the structure of radially symmetric solutions is preserved by the model dynamics: such property is indeed intrinsic to system (7.1), for which it can be proven analytically, and numerical evidence also emerges from the simulation results in Figure 15 and Figure 16, for example. Moreover, Figure 19 constitutes an experimental proof of the tendency to recover radially symmetric structures even starting from different initial configurations.

7.2. Three-dimensional experiments

The next step consists in exploring the three-dimensional framework, and we focus on the homogeneous invasion, in order to investigate the phenomenon of the spatial interstitial *gap* and its geometry. The COMSOL Multiphysics environment is still the principal resource for performing simulations, and we rely on ParaView – `https://www.paraview.org/` – for post-processing graphical results.

By analogy with the two-dimensional experiments, the 3-ball of radius R centered at the point C is chosen as simulation domain, and we build the corresponding finite element mesh as shown in Figure 12(B) for the volume $\Omega = \overline{B_R(C)}$ with $R = 3.5$ and $C = (0, 0, 0)$, for instance. The three-dimensional version of the initial profiles given in (7.3) is also considered, and $T = 7$ is assumed as final time instant. All the plots are realized by exploiting a graphical *heat map* and setting the color palette ranging from blue to red, as the magnitudes go from the lower values to the higher ones.

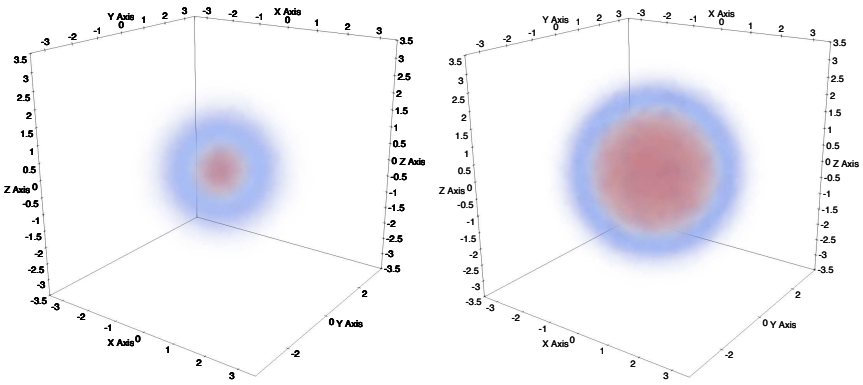

(a) *initial profile* (b) *intermediate time*

Figure 20: Tumour cells density evolution from the initial profile (A) towards an intermediate stage $T = 4$ (B).

As concerns the qualitative evolution, the resulting dynamics displays the cancerous peak spreading out at the expense of the local healthy tissue, that is what we have expected on the ground of the results previously described for the two-dimensional framework (refer to Section 7.1). Figure 20(A) shows the cancer cells initial profile, while Figure 20(B) reports the evaluation at an intermediate time

instant $T = 4$. By means of a transparency technique, that allows to appreciate the numerical data distribution throughout the three-dimensional volume, the tumour growth is suitably emphasized. The final configuration for both healthy and cancer cells densities is depicted in Figure 21(A) and Figure 21(B), respectively.

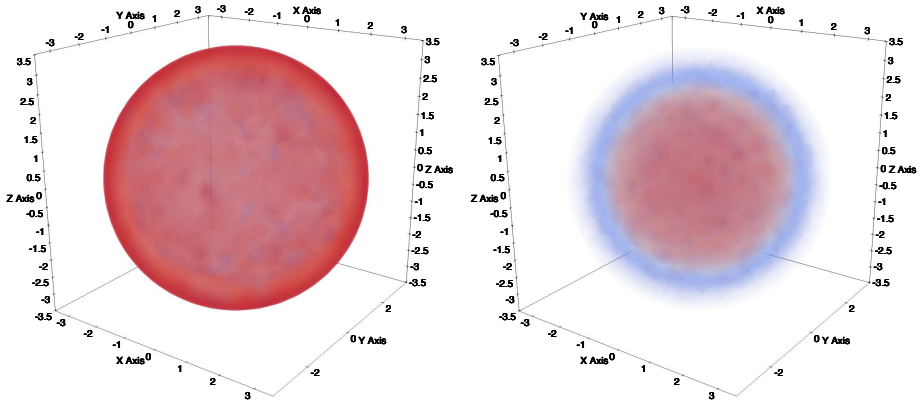

(a) *healthy cells density* (b) *tumour cells density*

Figure 21: Healthy and tumour cells densities evaluation at final time $T=7$.

For collecting information about the *gap* formation and understanding how the densities are actually distributed within the experimental domain, let us have a look inside the volumes plotted in Figure 21.

We cut the domain by means of a section plan passing through the origin and exploit the radial symmetry of the solutions to system (7.2) to state that any other section plan would produce similar results. We report in Figure 22 the graphs corresponding to the half ball for both healthy and tumour cells densities, where the numerical data under examination are represented on the external spherical surface only. This choice provides us with a clearer viewpoint to better detect the inner regions characterized by different density distributions. Indeed, taking advantage of symmetry arguments, we can easily infer that data distributions arising from surface representation retain an analogous behaviour inside any inner layer. Moreover, the healthy cells density is identically null throughout a ball contained inside the domain (see Figure 22(A)), while the innermost cancerous core reveals itself in bright red (see Figure 22(B)).

As a matter of fact, Figure 22 turns out to be a sort of *graphical proof* for assessing the presence of a separation zone between the healthy and cancer cells densities, preventing them from being in touch as the evolution is going on. Therefore, available space emerges to include the tumour cell density without producing intersection, as it has been already observed for the one-dimensional and the two-dimensional framework (see Figure 4(B) and Figure 18(B), respectively).

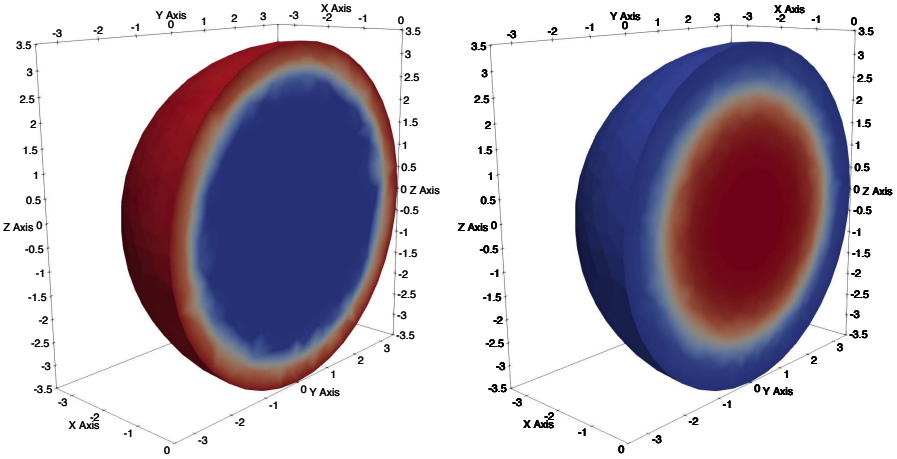

(a) *healthy cells density* (b) *tumour cells density*

Figure 22: The half balls arising from domain sectioning and provided with numerical data throughout the external spherical surface.

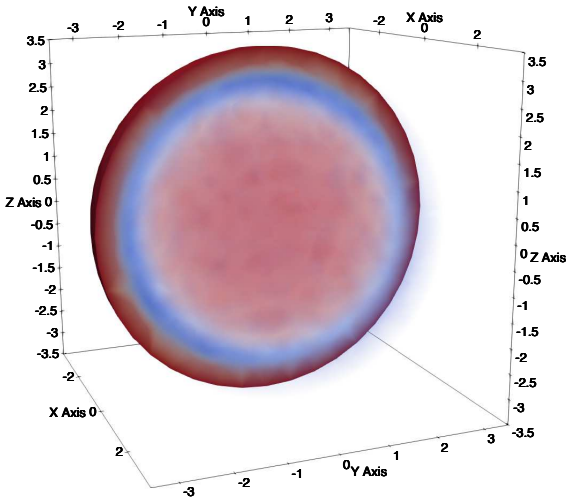

Figure 23: Three-dimensional tumour cells density profile located inside the half ball provided with healthy cells density data reproduced throughout the external spherical surface.

On that account, Figure 23 shows a simultaneous plot consisting of numerical data merging from Figure21(B) and Figure 22(A), where the cancerous core is placed in its corresponding spacial domain with respect to the half ball provided with the healthy cells density profile throughout the external spherical surface. At this stage, identifying the three-dimensional version of the spatial interstitial *gap* becomes possible: we are dealing with a null density solid shell located between the healthy and tumour cells profiles, which is quite well recognizable in Figure 23.
Finally, in order to provide the most effective three-dimensional representation of the qualitative dynamics of the Gatenby-Gawlinski model (7.1), we have realized a meaningful simultaneous plot of Figure 21(A) and Figure 21(B) by exploiting the transparency technique, and the resulting graph is depicted in Figure 24, where the geometry of the spatial interstitial *gap* is now clearly noticeable.

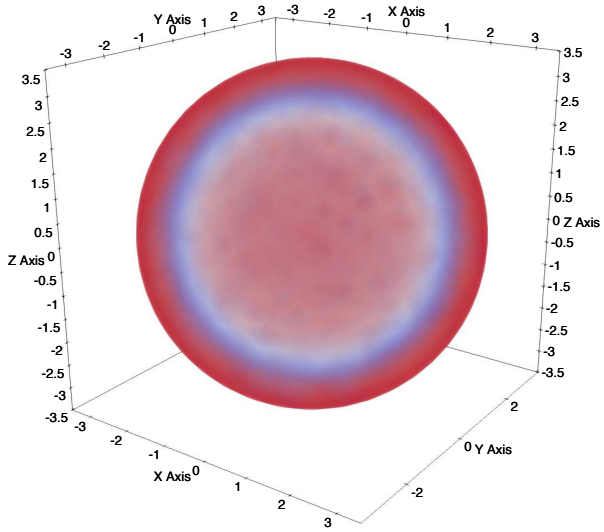

Figure 24: Detection of the three-dimensional spatial interstitial *gap* by means of the transparency technique.

8. Discussion and perspectives

In this article, the Gatenby-Gawlinski model for cancer invasion has been investigated by means of an analytically-supported numerical strategy.

First of all, a numerical algorithm based on finite volume approximations has been derived in the one-dimensional framework and validated for recovering simulation results related to biomedical features described in the literature [8, 11, 24]. The possibility of adopting integral formulations of the model system has inspired

such approach, to ensure accuracy in terms of closeness to the physics underlying the mathematical equations. We point out that, taking advantage of the general derivation performed in Section 3 for a semi-discrete scheme with variable spatial mesh size, our finite volume strategy well lends itself to be employed for further investigations on unstructured meshes [19].

Subsequently, we have focused on the qualitative aspects concerning the phenomenon of traveling fronts: specifically, the existence of an asymptotic wave speed has been experimentally proven by exploiting a space-averaged propagation speed estimate (refer to Section 4). This approximation, which turns out to be an original attempt within the theory of reaction-diffusion systems, has proven itself to be effective for recovering discrete estimates previously computed in [8, 24], for instance (through asymptotic and interpolation arguments), and it is particularly useful for its independence from the dynamics of the solutions to the model system.

Afterwards, by assuming suitable reduction hypotheses, in Section 6 we have derived a more manageable version of the Gatenby-Gawlinski model for further analytical investigations, thus opening the perspective also to reductions consisting of a single equation, that would be worth exploring in the framework of degenerate reaction-diffusion equations [32].

Finally, in Section 7 we have explored multidimensional configurations by opting for a finite element approach, with emphasis on the detection of the *gap* formation: two-dimensional as well as three-dimensional simulations have been carried out in order to contextualize its geometry and evolution in view of the biomedical applications. On the heels of these last achievements, the possibility of improving the computational effectiveness by introducing the *parallel computation paradigm* is doubtless very promising, so that more complex problems might be investigated for better reproducing realistic biomedical experiments (see [23], for example). Moreover, since numerical analysis and computational simulation of mathematical models in biology are nowadays an integral part of the research in this field, an effective visualisation of the results in necessary to provide an ideal platform on which biologists and mathematicians can communicate [7], hence we have also contributed to this issue in Section 7.2 dealing with challenging three-dimensional applications.

References

[1] Alberghina, L., Gaglio, D., Moresco, R.M., Gilardi, M.C., Messa, C., Vanoni, M.: A Systems Biology road map for the discovery of drugs targeting cancer cell metabolism, Curr. Pharm. Des. **20**, 2648-2666 (2014)

[2] Archetti, M.: Evolutionary dynamics of the Warburg effect: glycolysis as a collective action problem among cancer cells, J. Theor. Biol. **341**, 1-8 (2014)

[3] Astanin, S., Preziosi, L.: Mathematical modeling of the Warburg effect in tumour cords, J. Theor. Biol. **258**, 578-590 (2009)

[4] Bertuzzi, A., Fasano, A., Gandolfi, A., Sinisgalli, C.: Necrotic core in EMT6/Ro tumour spheroids: is it caused by an ATP deficit?, J. Theor. Biol. **262**, 142-150 (2010)

[5] Bianchini, L., Fasano, A.: A model combining acid-mediated tumour invasion and nutrient dynamics, Nonlinear Anal. Real World Appl. **10**(4), 1955-1975 (2009)
[6] Carmona-Fontaine, C., Bucci, V., Akkari, L., Deforet, M., Joyce, J.A., Xavier, J.B.: Emergence of spatial structure in the tumor microenvironment due to the Warburg effect, Proc. Natl. Acad. Sci. USA **110**, 19402-19407 (2013)
[7] Enderling, H., Anderson, A.R., Chaplain, M.A., Rowe, G.W.: Visualisation of the numerical solution of partial differential equation systems in three space dimensions and its importance for mathematical models in biology, Math. Biosci. Eng. **3**(4), 571-582 (2006)
[8] Fasano, A., Herrero, M.A., Rodrigo, M.R.: Slow and fast invasion waves in a model of acid-mediated tumour growth, Math. Biosci. **220**(1), 45-56 (2009)
[9] Folkman, J., Hochberg, M.: Self-regulation of growth in three dimensions, J. Exp. Med **38**, 745-753 (1973)
[10] Fouad, A.M.: A kinetic view of acid-mediated tumor invasion, Eur. Biophys. J. **47**(2), 185-189 (2018)
[11] Gatenby, R.A., Gawlinski, E.T.: A reaction-diffusion model of cancer invasion, Cancer Res. **56**, 5745-5753 (1996)
[12] Gatenby, R.A., Maini, P.K., Gawlinski, E.T.: Analysis of tumor as an inverse problem provides a novel theoretical framework for understanding tumor biology and therapy, Appl. Math. Lett. **15**, 339-345 (2002)
[13] Gatenby, R.A., Gawlinski, E.T.: The glycolytic phenotype in carcinogenesis and tumor invasion: insights through mathematical models, Cancer Res. **63**, 3847-3854 (2003)
[14] Gatenby, R.A., Gillies, R.J.: Why do cancers have high aerobic glycolysis?, Nat. Rev. Cancer **4**, 891-899 (2004)
[15] Gatenby, R.A., Gawlinski, E.T., Gmitro, A.F., Kaylor, B., Gillies, R.J.: Acid-meditated tumour invasion: a multidisciplinary study, Cancer Res. **66**, 5216-5223 (2006)
[16] Gatenby, R.A., Gillies, R.J.: Glycolysis in cancer: a potential target for therapy, Int. J. Biochem. Cell Biol. **39**, 1358-1366 (2007)
[17] Hadeler, K.P., Rothe, F.: Travelling fronts in nonlinear diffusion equations, J. Math. Biol. **2**, 251-263 (1975)
[18] Holder, A.B., Rodrigo, M.R., Herrero, M.A.: A model for acid-mediated tumour growth with nonlinear acid production term, Appl. Math. Comput. **227**, 176-198 (2014)
[19] Kolditz, O.: Computational methods in environmental fluid mechanics. Springer, Berlin, Heidelberg (2002)
[20] Lattanzio, C., Mascia, C., Plaza, R.G., Simeoni, C.: Analytical and numerical investigation of traveling waves for the Allen-Cahn model with relaxation, Math. Models Methods Appl. Sci. **26**, 931-985 (2016)
[21] Lattanzio, C., Mascia, C., Plaza, R.G., Simeoni, C.: Kinetic schemes for assessing stability of traveling fronts for the Allen-Cahn equation with relaxation. Appl. Numer. Math. **141**, 234-247 (2019)
[22] LeVeque, R.J., Yee, H.C.: A study of numerical methods for hyperbolic conservation laws with stiff source terms, J. Comput. Phys. **86**, 187-210 (1990)
[23] Màlaga, C., Minzoni, A., Plaza, R.G., Simeoni, C.: A chemotactic model for interaction of antagonistic microflora colonies: front asymptotics and numerical simulations, Stud. Appl. Math. **130**(3), 264-294 (2013)
[24] McGillen, J.B., Gaffney, E.A., Martin, N.K., Maini, P.K.: A general reaction-diffusion model of acidity in cancer invasion, J. Math. Biol. **68**(5), 1199-1224 (2014)
[25] Medina, M.Á.: Systems biology for molecular life sciences and its impact in biomedicine, Cell. Mol. Life Sci. **70**, 1035-1053 (2013)
[26] Medina, M.Á.: Mathematical modeling of cancer metabolism, Crit. Rev. Oncol. Hematol. **124**, 37-40 (2018)
[27] https://ngmedicine.com/could-cancer-be-a-metabolic-disease/
[28] Pera, D., Màlaga, C., Simeoni, C., Plaza, R.G.: On the efficient numerical simulation of heterogeneous anisotropic diffusion models for tumor invasion using GPUs, Rend. Mat. Appl. **7**, 23 pages, online first (2019)

[29] Perumpanani, A.J., Sherratt, J.A., Norbury, J., Byrne, H.M.: A two parameter family of travelling waves with a singular barrier arising from the modelling of the extracellular matrix mediated cellular invasion, Physica D: Nonlinear Phenomena **126**, 145-159 (1999)
[30] Quarteroni, A.: Numerical models for differential problems. Springer, Milano (2014)
[31] Quiroga, A.A., Fernández, D., Torres, G.A., Turner, C.V.: Adjoint method for a tumor invasion PDE-constrained optimization problem in 2D using adaptive finite element method, Appl. Math. Comput. **270**, 358-368 (2015)
[32] Sánchez-Garduño, F., Maini, P.K.: Traveling wave phenomena in some degenerate reaction-diffusion equations, J. Differential Equations **117**, 281-319 (1995)
[33] Shamsi, M., Saghafian, M., Dejam, M., Sanati-Nezhad, A.: Mathematical modeling of the function of Warburg effect in tumor microenvironment, Sci. Rep. Nature Publishing Group **8**, 1-12 (2018)
[34] Simeoni, C., Dinicola, S., Cucina, A., Mascia, C., Bizzarri, M.: Systems Biology approach and Mathematical Modeling for analyzing phase-space switch during epithelial-mesenchymal transition, Bizzarri M. (eds) Systems Biology, Methods in Molecular Biology **1702**, Humana Press, New York, 95-123 (2018)
[35] Smallbone, K., Gavaghan, D.J., Gatenby, R.A., Maini, P.K.: The role of acidity in solid tumour growth and invasion, J. Theor. Biol. **235**(4), 476-484 (2005)
[36] Smallbone, K., Gatenby, R.A., Maini, P.K.: Mathematical modelling of tumour acidity, J. Theor. Biol. **255**, 106-112 (2008)
[37] van Saarloos, W.: Front propagation into unstable states: marginal stability as a dynamical mechanism for velocity selection, Phys. Rev. A **37**(1), 211-229 (1988)
[38] Warburg, O.: The metabolism of tumors. Arnold Constable, London (1930)
[39] Warburg, O.: On the origin of cancer cells, Science **123**, 309-314 (1956)
[40] Wesseling, P.: Principles of computational fluid dynamics. Springer, Berlin, Heidelberg (2001)

Received: 23 February 2019/Accepted: 27 September 2019/Published online: 2 October 2019

Pierfrancesco Moschetta
Dipartimento di Matematica G. Castelnuovo, Sapienza Università di Roma, Piazzale Aldo Moro 2 - 00185 Roma (Italy).
moschetta@mat.uniroma1.it

Chiara Simeoni
Laboratoire de Mathématiques J.A. Dieudonné UMR CNRS 7351, Université de Nice Sophia-Antipolis, Parc Valrose 06108 Nice Cedex 02 (France).
simeoni@unice.fr